Toughening two dimensional materials through lattice disorder

Wenhui Xie
Institute of Mechanics, Chinese Academy of Sciences. University of Chinese Academy of Sciences.
Yujie Wei (yujie_wei@lnm.imech.ac.cn)
Institute of Mechanics, Chinese Academy of Sciences. University of Chinese Academy of Sciences. https://orcid.org/0000-0002-3213-7891
Huajian Gao
Nanyang Technological University https://orcid.org/0000-0002-8656-846X

Article

Keywords:

Posted Date: June 7th, 2022

DOI: https://doi.org/10.21203/rs.3.rs-1709665/v1

Abstract

Carbon-based two-dimensional (2D) materials, with graphene being the most prominent example, are some of the strongest materials existing today due to their covalent bonding but at the same time also the most fragile, with fracture toughness close to that of an ideally brittle solid, due to their intrinsic lack of effective dissipation mechanisms. Here, by investigating fracture mechanisms in monolayer amorphous carbon (MAC), we reveal a novel strategy to toughen 2D materials through lattice disorder. It is shown that lattice disorder results in nanoscale ripples which can alleviate stress concentration in the vicinity of crack-tips and render MAC flaw tolerant. Consequently, MAC outperforms graphene in resisting brittle fracture and endures larger strain to failure in the presence of a preexisting crack. Our work sheds light on the mechanisms of crack propagation in MAC and also provides a mechanistic basis for designing tough 2D materials through lattice disorder.

Introduction

Toughness, a measure of materials' resistance to fracture, depends on energy dissipation mechanisms in the vicinity of crack tips. The lack of mobile defects in two-dimensional (2D) graphene gives rise to its unprecedented high strength[1,2] at a cost of low resistance to crack propagation[3,4]. Its fracture toughness falls to a value close to that of an ideally brittle solid[5,6]. To increase the fracture toughness of brittle materials as strong as graphene while retaining its 2D nature, there are not many methods at our disposal. Theoretically, several promising approaches, including designing graphene structures with controlled distributions of topological defects[7–9], modifying the grain size[10,11] and misorientation angle of grain boundary[12–14], have been found to improve the fracture resistance of graphene. Turning those ideas into reality, however, has met significant challenges: atomic structures of 2D materials are difficult to be manipulated through mechanical exfoliation[15,16], chemical vapor deposition (CVD)[17–21], or other well-known technologies[22,23].

Recent success in synthesizing 2D free-standing monolayer amorphous carbon (MAC) at centimeter-scale[24] is a big stride toward topological defect engineering for 2D carbon. In contrast to the hexagonal lattice of graphene, MAC is a pure carbon structure with random crystalline islands surrounded by five-, six-, seven- and eight-member rings. Such single-layered carbon material with disordered lattice exhibits thermal stability at high temerpatures[25] and resistivity comparable to that of multiwall carbon nanotubes[26]. Furthermore, extremely high strength on the order of several gigapascals and large plastic-like strain can be achieved in layered 3D MAC composites[27]. In what follows, we report a novel fracture-toughening mechanism in MAC through the formation of three-dimensional configurations during the relaxation of its disordered lattice. The lattice disorder results in nanoscale ripples and subsequent fracture toughening, a strategy which may be applicable to many two-dimensional materials.

Results

The fracture behaviors of a pre-cracked sheet of MAC are explored using molecular dynamics (MD) simulations with well-calibrated potential (see Method - MD simulations for details). We first modelled crack propagation in a sample whose in-plane dimensions are 170 nm long by 150 nm wide where a central crack 20 nm long in the y direction is prepared. The stress-strain response of the cracked MAC at different temperatures is shown in Fig. 1a. Corresponding movies on crack dynamics are shown in Supplementary Movies (SM) 1 and 2. A nonlinear elastic response of MAC under tension is observed. The failure strength of pre-cracked samples, of both MAC and graphene, decreases linearly with the increase of temperature, as illustrated in Fig. 1b. The results for graphene are in agreement with previous investigations[10,28,29]. The snapshots of surface morphologies of the MAC sample deformed at 1 K and at strains of 0%, 5%, 15%, and 22%, are shown in Fig. 1c to f, respectively. The nonlinear stress-strain response of the pre-cracked MACs (Fig. 1a) originates from the geometrical reconfiguration. In free-standing mode, a disordered lattice under stress could reduce its energy through the formation of out-of-plane ripples, as seen in Fig. 1c. Flattening in ripples then serves as an ancillary mechanism of elastic deformation. The initial sharp crack, rather than extending under stress concentration, deforms with evident crack-blunting and becomes nearly circular prior to rupture (Fig. 1f).

Rippling accommodated crack-blunting is further explored in MAC samples of different initial crack-sizes. Figure 2 shows the mechanical responses of MAC and graphene samples containing distinct central cracks. We show in Figs. 2a and b the stress-strain curves of MAC and graphene at 1 K and 300 K. MAC samples with crack lengths from 3 nm to 50 nm all exhibit nonlinear stress-strain response at low strains and ductile-like failure at 1 K.

For both materials, their failure strength and failure strain decrease with increasing crack length, as demonstrated in Fig. 2c and d. Counterintuitively, the failure strength of pre-cracked MAC is greater than that of pre-cracked graphene at all crack lengths explored here, with an average difference up to 15 GPa at 1 K. Crack size has a much stronger influence on failure strength for pre-cracked MAC at 300 K. We can see from Fig. 2d that the failure strain of both materials follows a power-law with respect to the initial crack size. Besides, the failure strain of pre-cracked MAC is far greater than that of pre-cracked graphene.

A close comparison between the deformation patterns of MAC and graphene can help us understand the mechanisms that underlie their differences in strength and failure strain. We show in Fig. 3 the atomic stress contours of pre-cracked MAC with an initial crack of 3 nm (Figs. 3a, 3e), 20 nm (Figs. 3b, 3f), 40 nm (Figs. 3c, 3g) and pre-cracked graphene with an initial crack length of 20 nm (Figs. 3d, 3h), where we show in the top row (Figs. 3a-d) the status at half of the critical strain (the onset for crack propagation), and Figs. 3e-h at the bottom row are stress contour snapshots right before crack-extension. When the applied tensile strain is small, diffusive and homogeneous stress distribution is observed in pre-cracked MAC samples, in contrast to highly concentrated stress in the vicinity of the crack tip in graphene (see Fig. 3d). SM-3 and SM-4 show the stress distribution of a pre-cracked MAC and a pre-cracked graphene with an initial crack length of 6 nm during stretching. Due to the populous ‘defects’ in the disordered MAC, stress concentration at the crack tip is vastly alleviated (Fig. 3e) and the material becomes flaw-tolerant, in sharp contrast with its crystalline counterpart (see Fig. 3h). Ripples in MAC lead to enhanced ductility: the pre-cracked MAC exhibits a failure strain (before crack propagation) of 0.2, significantly greater than that of 0.08 in the pre-cracked graphene.

The physical limit of the Griffith criterion, i.e., when it fails to predict the fracture strength of materials with small nano-sized cracks, was found to be 10 nm in graphene, under which the Griffith strength is overestimated[30]. According to the Griffith criterion, the fracture stress σ_f for a stripe with a central crack of length $2a_0$ is given as[31,32]

$$\sigma_f = \frac{1}{F(\varphi)}\sqrt{\frac{E\Gamma}{\pi a}}$$

1

,

where E is the Young’s modulus, Γ the apparent fracture resistance of the crack plane, and $F(\varphi)$ is a geometrical factor in the form of

$$F(\varphi) = (1 - 0.025\varphi^2 + 0.06\varphi^4)\sqrt{\sec\left(\frac{\pi\varphi}{2}\right)}\text{, and } \varphi = \frac{2a_0}{W}\text{, (2)}$$

where W is the width of the stripe. For brittle materials, Γ corresponds to the surface energy of a 3D solids or edge energy of a 2D material. We show in Fig. 4 the failure strength and work-to-fracture of pre-cracked MAC and graphene samples, where φ ranges from 0 to 0.3 for a_0 explored here. The blue and red dashed lines in Fig. 4a come from theoretical predictions using Eq. (1), and the circular and square symbols stand for data from MD simulations. The magenta dashed line and triangular symbols are the maximum nominal strength (in the minimum cross-section) of the strip, $\sigma_{\text{th}}(a_0) = S(1-\varphi)$, where $S \approx 96$ GPa is the strength of non-cracked MAC at 1 K. We can see that the blue and magenta dashed lines intersect at $\varphi \approx 0.07$, corresponding to a crack length of 12 nm. For MAC samples with initial crack shorter than this length, the Griffith criterion no longer holds and the failure strength is governed by σ_{th}. This insensitivity to preexisting cracks demonstrates apparent flaw-tolerance[33] in MAC. In addition to the enhanced failure strength of MAC, its work-to-fracture is also much

greater than that of graphene (see Fig. 4b). The readers may refer to Table 1 for simulation details. Fracture toughness is related to the critical strain energy release rate through $G_{\mathrm{c}} = K_{\mathrm{c}}^2/E$, where $K_{\mathrm{c}} = F(\varphi) \bullet \sigma_{\mathrm{c}}\sqrt{\pi a_0}$ is the critical stress intensity factor for fracture. In contrast to the case of graphene, we see from Table 1 dramatically greater G_{c} of MAC. Its G_{c} at 1 K is higher than that at 300 K because of the ductile-like fracture at 1 K, as also shown in SM-1 and SM-2.

Table 1

Modelling details including crack size, critical fracture stress σ_{c} and energy release rate G_{c} of MAC and graphene with a pre-crack of length $2a_0$. Note greater value of G_{c} for MAC.

Crack	**Graphene 1 K**		**Graphene 300 K**		**MAC 1 K**		**MAC 300 K**	
$2a_0$ (nm)	σ_{c} (GPa)	$\sigma_{\mathrm{c}}\sqrt{a_0} \bullet F(\varphi)$ (MPa$\sqrt{\mathrm{m}}$)	σ_{c} (GPa)	$\sigma_{\mathrm{c}}\sqrt{a_0} \bullet F(\varphi)$ (MPa$\sqrt{\mathrm{m}}$)	σ_{c} (GPa)	$\sigma_{\mathrm{c}}\sqrt{a_0} \bullet F(\varphi)$ (MPa$\sqrt{\mathrm{m}}$)	σ_{c} (GPa)	$\sigma_{\mathrm{c}}\sqrt{a_0} \bullet F(\varphi)$ (MPa$\sqrt{\mathrm{m}}$)
3	58.78	2.28	62.75	2.43	94.61	3.66	86.40	3.35
6	54.26	2.97	51.00	2.80	76.48	4.19	63.41	3.48
12	44.28	3.44	39.83	3.10	66.74	5.18	55.18	4.29
20	36.08	3.64	33.08	3.34	56.77	5.72	50.38	5.08
30	26.03	3.26	26.42	3.31	50.79	6.33	28.26	3.52
40	18.92	2.79	24.87	3.67	44.63	6.52	30.13	4.40
50	9.65	1.65	11.30	1.91	41.98	6.99	25.54	4.25
G_{c} (J/m^2)	25.72		27.09		207.69		112.12	

Due to the typical nonlinear behavior of pre-cracked MAC during stretching (see Fig. 1a and Fig. 2a), we adopt the domain J-integral method[34,35] to quantify the fracture resistance of cracked MAC samples. We show in Fig. 5a the defined domain and related parameters for the integration (see Methods - Domain J-integral at the atomic scale).

The domain J-integral from more than ten integral domains with different r_1 and r_2 are illustrated in Fig. 5b. For the sake of clarity, we choose r_1 and r_2 between 0.15 and 0.45 of the crack length. The average J-integral of MAC is $65.4 \pm 2.8 \mathrm{J/m}^2$ at 1 K and $56.5 \pm 1.6 \mathrm{J/m}^2$ at 300 K, while that of graphene is $10.9 \pm 1.0 \mathrm{J/m}^2$ at 1 K and $10.1 \pm 1.3 \mathrm{J/m}^2$ at 300 K. It can be observed that the J-integral of pre-cracked MAC at both 1 K and 300 K is approximate six times those of pre-cracked graphene, and the J-integral of pre-cracked MAC at 1 K is slightly higher than that at 300 K, which are consistent with the energy release rate G_c shown in Table 1. The domain J-integral applied to analyze the fracture properties of atomically thin MAC and graphene seems much better than the contour-based J-integral, given the discrete nature of MD simulations for these materials.

Discussion

The substantially enhanced resistance to fracture in MAC in comparing against graphene can be attributed to its populous defects near a crack tip, which leads to crack-trapping and mitigation of local stress concentration. In this sense, the atomic defects related to lattice disorder in MAC, often regarded as Achilles heels in stressed materials, offer a unique feature rarely seen in bulk materials. Defect-borne stresses in free-standing monolayers give rise to three-dimensional nanoscale ripples[7,36–38], which contribute to better deformability and can be generalized to other thin structures. To verify this conjecture,

we intentionally generate monolayer graphene with out-of-plane domes characterized by an amplitude h and a periodic space λ. In Fig. 6a, we show a graphene with repeated domes. For detailed simulation data, please refer to Table 2. We then cut a 3 nm edge-crack in the samples. Figures 6d to f describe the stress evolution in the pre-cracked graphene with domes, where ultralow stress concentration at the crack tip is realized. Figures. 6h and i are surface morphologies corresponding to Figs. 6d and f, respectively. All samples have a failure strength up to ~ 50 GPa and a failure strain far greater than that of flat graphene, as seen in Fig. 6g. Under stretching, the distributed ripples (domes) are gradually flattened (see Figs. 6h to i), giving rise to large plastic-like deformation without crack propagation, a behavior not possible in the case of a flat graphene (Fig. 6b to c). The dynamic process of crack propagation in these two structures are shown in SM-5 and SM-6. The toughness of sinusoidally domed graphene increases with increasing wavelength, as shown in Table 2.

Table 2

Simulation data of wavelength-amplitude ratio λ/h, critical fracture stress σ_c and energy release rate $G_c = \left(1.14\sigma_{\mathrm{c}}\sqrt{\pi a_0}\right)^2/E$ for sinusoidally domed graphene with a single-edged pre-crack of length $a_0 = 3\mathrm{nm}$.

λ/h	σ_{c} (GPa)	$\sigma_{\mathrm{c}}\sqrt{a_0}$ (MPa$\sqrt{\mathrm{m}}$)	E (GPa)	G_{c} (J/m^2)
5.4	48.81	2.67	488	59.80
6.4	50.20	2.75	427	72.29
7.7	49.98	2.74	364	84.06
9.0	52.67	2.88	395	86.02
∞ (flat)	50.84	2.78	1000	31.66

The monolayer graphene with out-of-plane domes serves as a demonstration of the generality of the underlying nano-ripple mechanism to enhance fracture toughness in 2D materials. Practically, to scale up the process while retaining the ultra-high flexibility of 2D materials, one may introduce disturbances to the conventional routines for 2D material synthesis, e.g., laser assistance chemical vapor deposition to make centimeter-scale MAC[24]. It is worth noting that disordered lattice is not necessary for an entire sheet, rather it can be selectively introduced near vulnerable regions – edges, corners, connecting junctions, and sites of potential stress concentration to enhance the mechanical reliability of a structure or device. Alternatively, one may consider preparing single layer 2D materials by doping embedded domains of high fracture toughness through lattice mixture[39,40], or through supplanting carbon patches with regions of distinct elements[41-43], in resemblance to patterns seen in a pepperoni pizza. Such strategies, while extremely challenging, are under development.

To conclude, inspired by the outstanding properties of MAC[27], we demonstrate that pre-cracked MAC exhibits anomalous ductile fracture. Furthermore, the nominal strength of pre-cracked MACs is relatively insensitive to crack length, indicating that they are more flaw-tolerant[44-47]. It is worth noting that the failure strength and failure strain of pre-cracked MAC are much higher than that of pre-cracked graphene at any crack length, which can be attributed to more uniform stress distribution and therefore lower level stress concentration in pre-cracked MAC under stretching. In addition, crack shielding as a result of rippling leads to crack trapping and the enhancement of resistance to fracture in pre-cracked MAC. Such geometrical features may be employed and be generalized to enhance fracture resistance of other 2D materials and thin sheets.

Methods

MD simulations

For samples with an initial central crack, their in-plane dimensions are about 170 nm long by 150 nm wide. The MD package LAMMPS[48] (large-scale atomic/molecular massively parallel simulator) is adopted for modelling. All simulations are performed under the NPT ensemble for structure relaxation and NVT ensemble during stretching. Periodic boundary condition is applied along the horizontal and vertical directions, and out-of-plane deformation is set free. For all simulations, the Adaptive Intermolecular Reactive Empirical Bond Order (AIREBO) Potential for carbon and a constant time step of 1 femtosecond are used. The cutoff distance is set to 1.92 Å, as suggested by previous studies[38,49,50]. All samples are strained at a strain rate $10^9 \mathrm{s}^{-1}$.

For samples with an initial edge crack, the in-plane dimensions are 77 nm by 103 nm. The NPT ensemble and periodic boundary condition are applied during structure relaxation. Tension is achieved by applying a constant velocity 0.5 Å/ps to a group of boundary atoms along y direction. During stretching, the NVT and NVE ensembles are applied to the mobile and fixed atom groups, respectively.

Domain J-integral at the atomic scale

One of the equivalent forms of the J-integral is a closed contour integral of the strain energy density and work done by tractions on the contour[51]

$$J = \int_{\Gamma} \left(W_S \delta_{1j} - \sigma_{ij} \frac{\partial u_i}{\partial x_1} \right) n_j \mathrm{d}\Gamma$$

3

,

where W_S is the strain energy density, σ_{ij} and u_i are the stress and displacement components respectively, n_j is the unit outward normal to the contour. The subscript '1' in the above equation denotes the direction parallel to the crack, which is along the $y-$direction, as seen in Fig. 5a, where the integral path Γ and related parameters are also identified. Since the atomic model is a discrete system, contour integration cannot be performed. Therefore, an equivalent domain J-integral method is adopted here. The contour J-integral in Eq. (3) is now written in equivalence with the domain J-integral in the blue region in Fig. 5a, which is written in the form of [34,35]

$$J = \int_{A} \left(W_S \delta_{1j} - \sigma_{ij} \frac{\partial u_i}{\partial x_1} \right) q_{,j} \mathrm{d}A$$

4

.

Where q is a smooth function in domain A, which equals to 1 on Γ and vanishes on C_1. It has been demonstrated that J is insensitive to the format of q-functions. For simplicity and without loss of accuracy, we adopt a linear variation of q with r:

$$q = (r_2 - r)/(r_2 - r_1). \, (5)$$

We may rewrite Eq. (4)—after coordinate transformation—as follows

$$J = \int_{A} \left[\left(w - \sigma_{22} \frac{\partial v}{\partial y} - \sigma_{12} \frac{\partial u}{\partial y} \right) q_{,2} - \left(\sigma_{21} \frac{\partial v}{\partial y} + \sigma_{11} \frac{\partial u}{\partial y} \right) q_{,1} \right] \mathrm{d}A$$

6

.

We use an algorithm similar to finite element method to calculate the domain J-integral of a discrete MD sample. Quadrilateral isoperimetric elements with four nodes are used for numerical integration. Eq. (6) in discretized form is given as

$$J = \sum_{iE=1}^{NE} \left[\left(w^{iE} - \sigma_{22}^{iE} \frac{\partial v}{\partial y}^{iE} - \sigma_{12}^{iE} \frac{\partial u}{\partial y}^{iE} \right) q_{,2}^{iE} - \left(\sigma_{21}^{iE} \frac{\partial v}{\partial y}^{iE} + \sigma_{11}^{iE} \frac{\partial u}{\partial y}^{iE} \right) q_{,1}^{iE} \right] \mathrm{d}A^{iE}$$

7

,

where NE is the total number of elements in the domain, and w^{iE} the strain energy density, which is obtained by counting the potential energy difference before and after deformation:

$$w^{iE} = \left[\sum_{iN=1}^{NN} \left(Pe^{iN} - Pe_0^{iN} \right) \right] / V^{iE}, V^{iE} = \mathrm{d}A^{iE} \bullet t. \text{ (8)}$$

Here NN is the number of atoms in the element iE, Pe_0^{iN} and Pe^{iN} are the potential energy of the atom iN before and after deformation, respectively, V^{iE} is the volume of element iE and $t = 0.34\mathrm{nm}$ is the thickness of MAC and graphene. The element area $\mathrm{d}A^{iE}$ is given as

$$\mathrm{d}A^{iE} = \frac{1}{2} \mathrm{d}\theta \bullet \left[(r + \mathrm{d}r)^2 - r^2 \right]$$

9

.

Stresses of the element iE are the volumetric average among atoms in the element, $\sigma_{kl}^{iE} = \left(-\sum_{iN=1}^{NN} S_{kl}^{iN} \right) / V^{iE}$, where S_{kl}^{iN} is the kl stress component of atom iN at current step.

We calculate the derivatives $\frac{\partial u}{\partial y}^{iE}$, $\frac{\partial v}{\partial y}^{iE}$and $q_{,j}^{iE}$ using a two-dimensional Gaussian integral with two integration points in each direction. The average atomic displacements within the radius NR are taken as the nodal displacements u_i, v_i, i=1,…4. For $NR = 0.4$ nm, there are about 20 atoms associated with a node. The strains and $q_{,j}$ at the Gauss integration points (ξ, η) are then calculated as

$$\epsilon_x (\xi, \eta) = \frac{\partial u}{\partial y} = \sum_{i=1}^{4} (\partial N_i / \partial y) \bullet u_i$$

10a

,

$$\epsilon_y (\xi, \eta) = \frac{\partial v}{\partial y} = \sum_{i=1}^{4} (\partial N_i / \partial y) \bullet v_i$$

10b

,

$$q_{,1} (\xi, \eta) = \frac{\partial q}{\partial x} = \sum_{i=1}^{4} (\partial N_i / \partial x) \bullet q_i$$

10c

,

$$q_{,2} (\xi, \eta) = \frac{\partial q}{\partial y} = \sum_{i=1}^{4} (\partial N_i / \partial y) \bullet q_i$$

10d

,

and the shape function is given as $N_i = \frac{1}{4}(1+\xi_i\xi)(1+\eta_i\eta)$. Mapping between an element natural coordinate and the global Cartesian coordinate is

$x = \sum_{i=1}^{4} N_i^{'} x_i$, $y = \sum_{i=1}^{4} N_i^{'} y_i$, (11)

where x_i and y_i are the coordinates of the element nodes in the global coordinate system, and $N_i^{'} = N_i$ for quadrilateral isoperimetric elements. Therefore, we have

$$\begin{bmatrix} \partial N_i/\partial x \\ \partial N_i/\partial y \end{bmatrix} = \boldsymbol{J}_{\mathrm{m}}{}^{-1} \begin{bmatrix} \partial N_i/\partial \xi \\ \partial N_i/\partial \eta \end{bmatrix}, \tag{12}$$

where the Jacobian matrix $\boldsymbol{J}_{\mathrm{m}}$ given as

$$\boldsymbol{J}_{\mathrm{m}} = \begin{bmatrix} \partial x/\partial \xi & \partial y/\partial \xi \\ \partial x/\partial \eta & \partial y/\partial \eta \end{bmatrix}. \tag{13}$$

Finally, the elemental displacement derivatives can be given as

$$\frac{\partial u^{iE}}{\partial y} = \frac{1}{A}\int_A \varepsilon_x dA = \frac{1}{A}\int_{-1}^{1}\int_{-1}^{1} \varepsilon_x |\boldsymbol{J}_{\mathrm{m}}| d\xi d\eta$$
$$= \frac{1}{A}\sum_{i=1,2}\sum_{j=1,2} \varepsilon_x(\xi_i,\eta_j)\cdot\left|\boldsymbol{J}_{\mathrm{m}}(\xi_i,\eta_j)\right|\cdot H_i \cdot H_j, \tag{14a}$$

$$\frac{\partial v^{iE}}{\partial y} = \frac{1}{A}\int_A \varepsilon_y dA = \frac{1}{A}\int_{-1}^{1}\int_{-1}^{1} \varepsilon_y |\boldsymbol{J}_{\mathrm{m}}| d\xi d\eta$$
$$= \frac{1}{A}\sum_{i=1,2}\sum_{j=1,2} \varepsilon_y(\xi_i,\eta_j)\cdot\left|\boldsymbol{J}_{\mathrm{m}}(\xi_i,\eta_j)\right|\cdot H_i \cdot H_j, \tag{14b}$$

and those of $q_{,j}$ are

$$q_{,1}^{iE} = \frac{1}{A}\sum_{i=1,2}\sum_{j=1,2} q_{,1}(\xi_i,\eta_j)\cdot\left|\boldsymbol{J}_{\mathrm{m}}(\xi_i,\eta_j)\right|\cdot H_i \cdot H_j, \tag{14c}$$

$$q_{,2}^{iE} = \frac{1}{A}\sum_{i=1,2}\sum_{j=1,2} q_{,2}(\xi_i,\eta_j)\cdot\left|\boldsymbol{J}_{\mathrm{m}}(\xi_i,\eta_j)\right|\cdot H_i \cdot H_j, \tag{14d}$$

for

$$A = \int_A dA = \int_{-1}^{1}\int_{-1}^{1} |\boldsymbol{J}_{\mathrm{m}}|\, d\xi d\eta = \sum_{i=1,2}\sum_{j=1,2}\left|\boldsymbol{J}_{\mathrm{m}}(\xi_i,\eta_j)\right|\cdot H_i \cdot H_j, \tag{14e}$$

where H_i and H_{j} are the weights at the Gaussian integration points, $H_i = H_j = 1$ here. By the end, we obtain the domain J-integral by substituting Eqs. (8) and (14) into Eq. (7).

Data availability

The authors declare that the main data supporting the results of this work are contained within the paper and its associated Supplementary Information. All other relevant data are available from the corresponding author upon reasonable request.

Declarations

Acknowledgement

Y.W. acknowledges support from the NSFC Basic Science Center Program for ‘Multiscale Problems in Nonlinear Mechanics’ (Grant No. 11988102). H.G. acknowledges a research startup grant (002479-00001) from Nanyang Technological University

and the Agency for Science, Technology and Research (A*STAR) in Singapore.

Author contributions

Y.W. and H.G. conceived the project; W.X. carried out the simulations. All authors analyzed data, discussed the results, wrote and edited the manuscript.

Competing interests

The authors declare no competing interests.

References

1. Liu, F., Ming, P. & Li, J. Ab initiocalculation of ideal strength and phonon instability of graphene under tension. Phys. Rev. B **76**, 064120, doi:10.1103/PhysRevB.76.064120 (2007).
2. Lee, C., Wei, X., Kysar, J. W. & Hone, J. Measurement of the elastic properties and intrinsic strength of monolayer graphene. Science **321**, 385–388, doi:10.1126/science.1157996 (2008).
3. Budarapu, P. R. *et al.* Crack propagation in graphene. J. Appl. Phys. **118**, doi:10.1063/1.4928316 (2015).
4. Lopez-Polin, G., Gomez-Herrero, J. & Gomez-Navarro, C. Confining crack propagation in defective graphene. Nano Lett. **15**, 2050–2054, doi:10.1021/nl504936q (2015).
5. Zhang, P. *et al.* Fracture toughness of graphene. Nat. Commun. **5**, 3782, doi:10.1038/ncomms4782 (2014).
6. Zhang, T., Li, X. & Gao, H. Fracture of graphene: a review. Int. J. Fract. **196**, 1–31, doi:10.1007/s10704-015-0039-9 (2015).
7. Zhang, T., Li, X. & Gao, H. Designing graphene structures with controlled distributions of topological defects: A case study of toughness enhancement in graphene ruga. Extreme Mech. Lett. **1**, 3–8, doi:10.1016/j.eml.2014.12.007 (2014).
8. Wang, M. C., Yan, C., Ma, L., Hu, N. & Chen, M. W. Effect of defects on fracture strength of graphene sheets. Comput. Mater. Sci. **54**, 236–239, doi:10.1016/j.commatsci.2011.10.032 (2012).
9. Rajasekaran, G., Narayanan, P. & Parashar, A. Effect of Point and Line Defects on Mechanical and Thermal Properties of Graphene: A Review. Crit. Rev. Solid State **41**, 47–71, doi:10.1080/10408436.2015.1068160 (2015).
10. Chen, M. Q. *et al.* Effects of grain size, temperature and strain rate on the mechanical properties of polycrystalline graphene – A molecular dynamics study. Carbon **85**, 135–146, doi:10.1016/j.carbon.2014.12.092 (2015).
11. Shekhawat, A. & Ritchie, R. O. Toughness and strength of nanocrystalline graphene. Nat. Commun. **7**, 10546, doi:10.1038/ncomms10546 (2016).
12. Li, X. & Guo, J. Numerical investigation of the fracture properties of pre-cracked monocrystalline/polycrystalline graphene sheets. Materials **12**, 263, doi:10.3390/ma12020263 (2019).
13. Wang, Y. & Liu, Z. The fracture toughness of graphene during the tearing process. Model. Simul. Mater. Sc. **24**, doi:10.1088/0965-0393/24/8/085002 (2016).
14. Rasool, H. I., Ophus, C., Klug, W. S., Zettl, A. & Gimzewski, J. K. Measurement of the intrinsic strength of crystalline and polycrystalline graphene. Nat. Commun. **4**, doi:10.1038/ncomms3811 (2013).
15. Novoselov, K. S. *et al.* Two-dimensional atomic crystals. *Proc. Natl. Acad. Sci. USA* **102**, 10451–10453, doi:10.1073/pnas.0502848102 (2005).
16. Novoselov, K. S. *et al.* Electric field effect in atomically thin carbon films. Science **306**, 666–669, doi:10.1126/science.1102896 (2004).
17. Sutter, P. W., Flege, J. I. & Sutter, E. A. Epitaxial graphene on ruthenium. Nat. Mater. **7**, 406–411, doi:10.1038/nmat2166 (2008).
18. Kim, K. S. *et al.* Large-scale pattern growth of graphene films for stretchable transparent electrodes. Nature **457**, 706–710, doi:10.1038/nature07719 (2009).

19. Li, X. *et al.* Large-area synthesis of high-quality and uniform graphene films on copper foils. Science **324**, 1312–1314, doi:10.1126/science.1171245 (2009).
20. Arco, L. G. D. *et al.* Continuous, highly flexible, and transparent graphene films by chemical vapor deposition for organic photovoltaics. ACS Nano **4**, 2865–2873, doi:10.1021/nn901587x (2010).
21. Lee, S., Lee, K. & Zhong, Z. Wafer scale homogeneous bilayer graphene films by chemical vapor deposition. Nano Lett. **10**, 4702–4707, doi:10.1021/nl1029978 (2010).
22. Guo, Y. *et al.* General route toward patterning of graphene oxide by a combination of wettability modulation and spin-coating. ACS Nano **4**, 5749–5754, doi:10.1021/nn101463j (2010).
23. Emtsev, K. V. *et al.* Towards wafer-size graphene layers by atmospheric pressure graphitization of silicon carbide. Nat. Mater. **8**, 203–207, doi:10.1038/nmat2382 (2009).
24. Toh, C. T. *et al.* Synthesis and properties of free-standing monolayer amorphous carbon. Nature **577**, 199–203, doi:10.1038/s41586-019-1871-2 (2020).
25. Júnior, M. L. P., Cunha, W. F., Galvão, D. S. & Júnior, L. A. R. A reactive molecular dynamics study on the mechanical properties of a recently synthesized amorphous carbon monolayer converted into a nanotube/nanoscroll. Phys. Chem. Chem. Phys. **23**, 9089–9095, doi:10.1039/d0cp06613c (2021).
26. Hayashi, T. *et al.* A reversible strain-induced electrical conductivity in cup-stacked carbon nanotubes. Nanoscale **5**, 10212–10218, doi:10.1039/c3nr01887c (2013).
27. Xie, W. & Wei, Y. Roughening for strengthening and toughening in monolayer carbon based composites. Nano Lett. **21**, 4823–4829, doi:10.1021/acs.nanolett.1c01462 (2021).
28. Zhang, Y. Y. & Gu, Y. T. Mechanical properties of graphene: Effects of layer number, temperature and isotope. Comput. Mater. Sci. **71**, 197–200, doi:10.1016/j.commatsci.2013.01.032 (2013).
29. Zhao, H. & Aluru, N. R. Temperature and strain-rate dependent fracture strength of graphene. J. Appl. Phys. **108**, doi:10.1063/1.3488620 (2010).
30. Yin, H. *et al.* Griffith criterion for brittle fracture in graphene. Nano Lett. **15**, 1918–1924, doi:10.1021/nl5047686 (2015).
31. Griffith, A. A. The phenomena of rupture and flow in solids. Phil. Trans. R. Soc. Lond. A **221**, 163–198, doi:10.1098/rsta.1921.0006 (1921).
32. Bazant, Z. E. & Planas, J. in *New Directions in Civil Engineering Fracture and size effect: in concrete and other quasi brittle materials* (ed Taylor & Francis) (CRC Press, 1998).
33. Zhang, T., Li, X., Kadkhodaei, S. & Gao, H. Flaw insensitive fracture in nanocrystalline graphene. Nano Lett. **12**, 4605–4610, doi:10.1021/nl301908b (2012).
34. Cueto-Felgueroso, C. in *Structural Mechanics in Reactor Technology 16th* (Washington DC, 2001).
35. Breitbarth, E., Strohmann, T., Besel, M. & Reh, S. Determination of stress intensity factors and j integral based on digital image correlation. Frattura ed Integrità Strutturale **13**, 12–25, doi:10.3221/igf-esis.49.02 (2019).
36. Chang, Z., Yang, R. & Wei, Y. The linear-dependence of adhesion strength and adhesion range on temperature in soft membranes. J. Mech. Phys. Solids **132**, doi:10.1016/j.jmps.2019.103697 (2019).
37. Wei, Y., Wang, B., Wu, J., Yang, R. & Dunn, M. L. Bending rigidity and Gaussian bending stiffness of single-layered graphene. Nano Lett. **13**, 26–30, doi:10.1021/nl303168w (2013).
38. Wei, Y. *et al.* The nature of strength enhancement and weakening by pentagon-heptagon defects in graphene. Nat. Mater. **11**, 759–763, doi:10.1038/nmat3370 (2012).
39. Mendoza, M. E. *et al.* Revealing lattice disorder, oxygen incorporation and pore formation in laser induced two-photon oxidized graphene. Carbon **143**, 720–727, doi:10.1016/j.carbon.2018.11.070 (2019).
40. Lv, R. *et al.* Ultrasensitive gas detection of large-area boron-doped graphene. *Proc. Natl. Acad. Sci. USA* **112**, 14527–14532, doi:10.1073/pnas.1505993112 (2015).

41. Lin, P. C. *et al.* Doping Graphene with Substitutional Mn. ACS Nano **15**, 5449–5458, doi:10.1021/acsnano.1c00139 (2021).
42. Wang, H. *et al.* Doping monolayer graphene with single atom substitutions. Nano Lett. **12**, 141–144, doi:10.1021/nl2031629 (2012).
43. Zhang, C. *et al.* Synthesis of nitrogen-doped graphene using embedded carbon and nitrogen sources. Adv. Mater. **23**, 1020–1024, doi:10.1002/adma.201004110 (2011).
44. Gao, H., Ji, B., Ja¨ger, I. L., Arzt, E. & Fratzl, P. Materials become insensitive to flaws at nanoscale: Lessons from nature. *Proc. Natl. Acad. Sci. USA* **100**, 5597–5600, doi:10.1073/pnas.0631609100 (2003).
45. Gao, H., Ji, B., Buehler, M. J. & Yao, H. Flaw tolerant bulk and surface nanostructures of biological systems. Mechanics & Chemistry of Biosystems Mcb **1**, 37–52 (2004).
46. Ji, B., Gao, H. & Wang, T. Flow stress of biomorphous metal–matrix composites. Mater. Sci. Eng. A **386**, 435–441, doi:10.1016/s0921-5093(04)01000-7 (2004).
47. Buehler, M. J., Yao, H., Gao, H. & Ji, B. Cracking and adhesion at small scales: atomistic and continuum studies of flaw tolerant nanostructures. Model. Simul. Mater. SC **14**, 799–816, doi:10.1088/0965-0393/14/5/001 (2006).
48. Plimpton, S. Fast parallel algorithms for short-range molecular dynamics. J. Comput. Phys. **117**, 1–19, doi:10.1006/jcph.1995.1039 (1995).
49. Shenderova, O. A., Brenner, D. W., Omeltchenko, A., Su, X. & Yang, L. H. Atomistic modeling of the fracture of polycrystalline diamond. Phys. Rev. B **61**, 3877, doi:10.1103/PhysRevB.61.3877 (2000).
50. Zhao, H., Min, K. & Aluru, N. R. Size and chirality dependent elastic properties of graphene nanoribbons under uniaxial tension. Nano Lett. **9**, 3012–3015, doi:10.1021/nl901448z (2009).
51. RICE, J. R. A path independent integral and the approximate analysis of strain concentration by notches and cracks. J. Appl. Mech. **35**, 379–386 (1968).

Figures

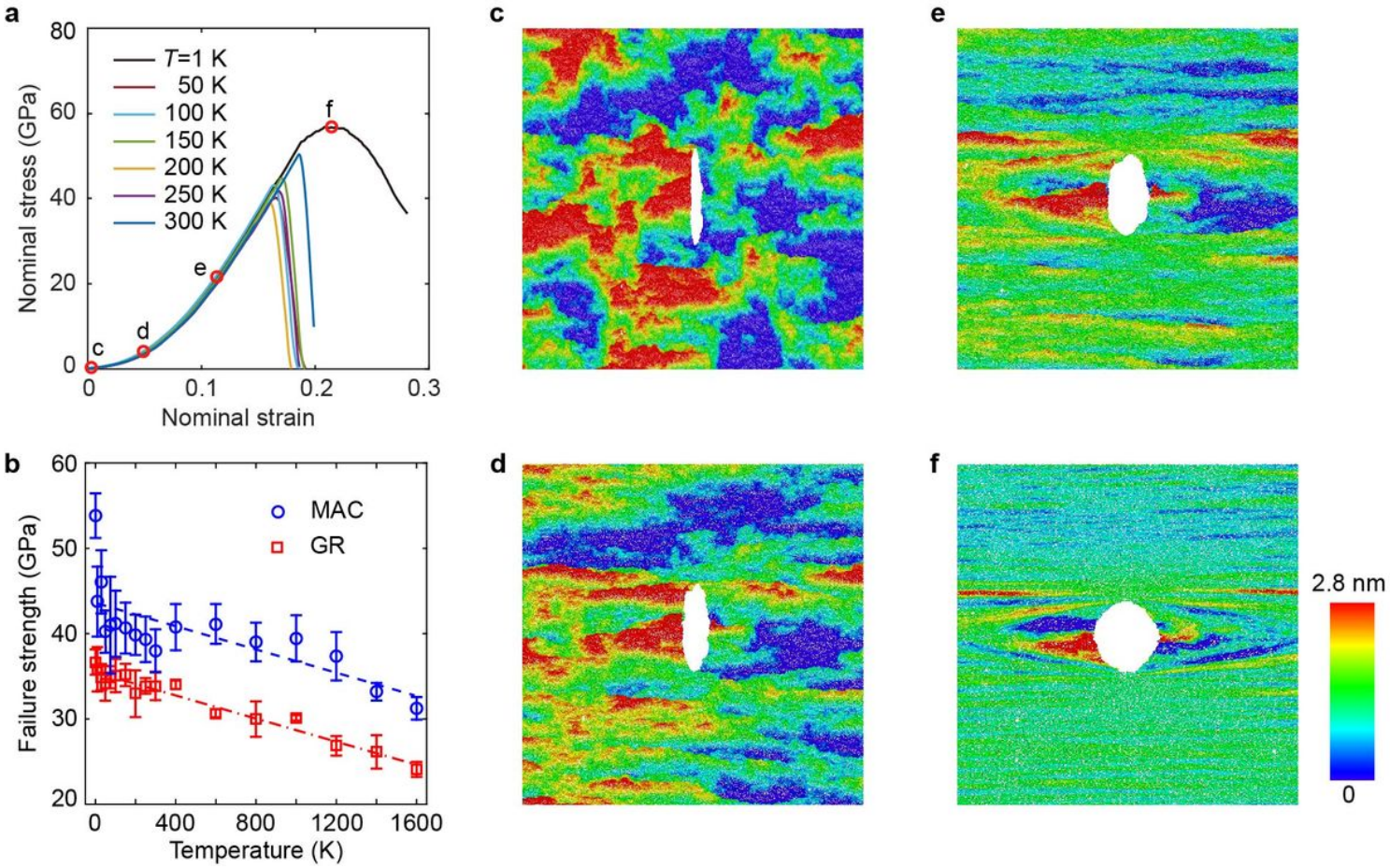

Figure 1

Temperature-dependent mechanical behavior of a pre-cracked sheet of MAC. (a) Uniaxial tensile stress-strain curves of the pre-cracked MAC with a central crack of length nm. (b) Failure strength as a function of temperature in the pre-cracked MAC and graphene (Error bar comes from three independent samples). (c) to (f) Snapshots of the deformed sample at different strains keyed in (a): (c) ε = 0, (d) ε = 0.05, (e) ε = 0.15, and (f) ε = 0.22.

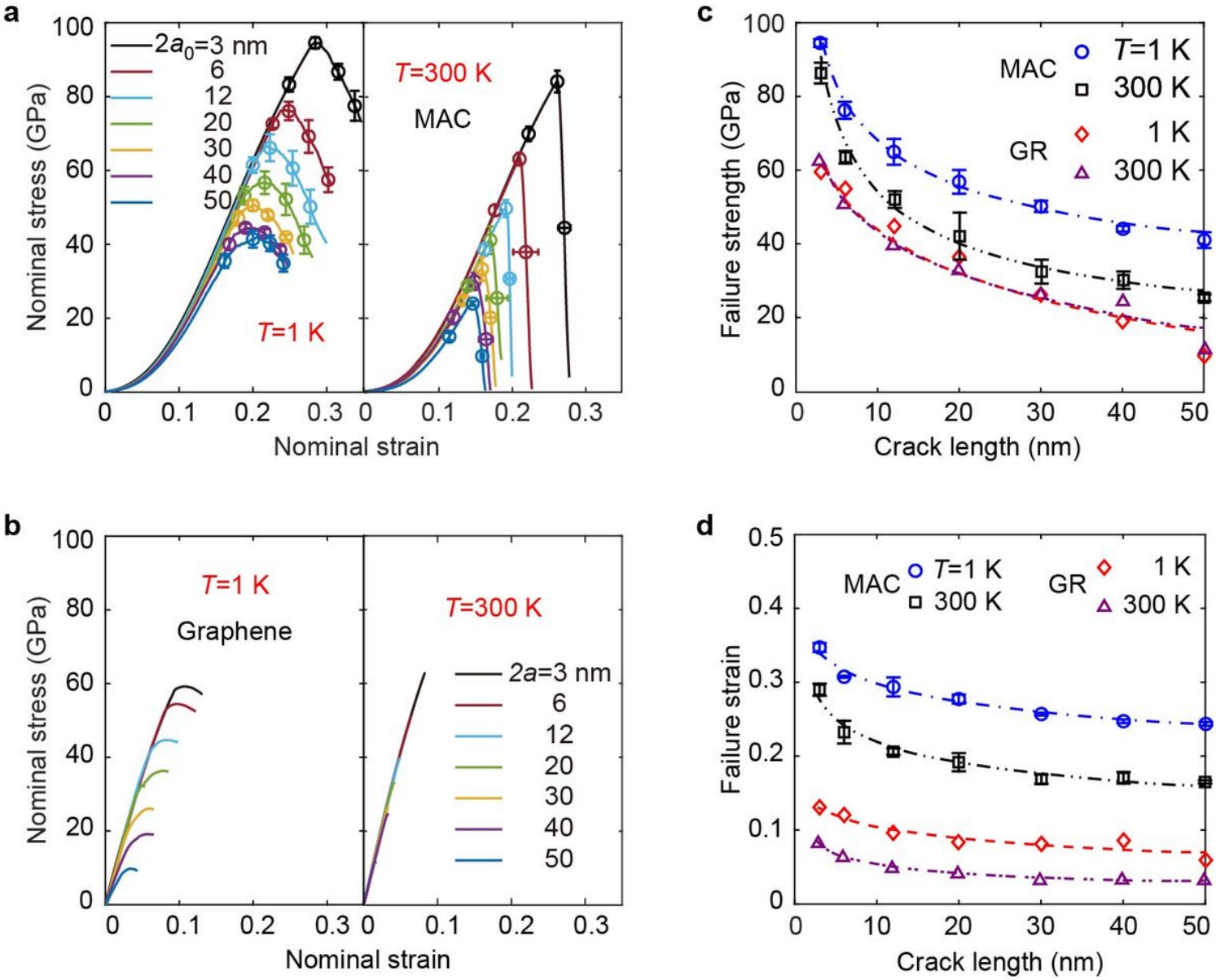

Figure 2

Crack-size dependent failure in MAC and graphene. Stress-strain curves of pre-cracked (a) MAC and (b) graphene under tension at 1 K (left) and 300 K (right). (c) Failure strength and (d) failure strain as functions of crack length (Error bar: standard deviation of three MAC samples).

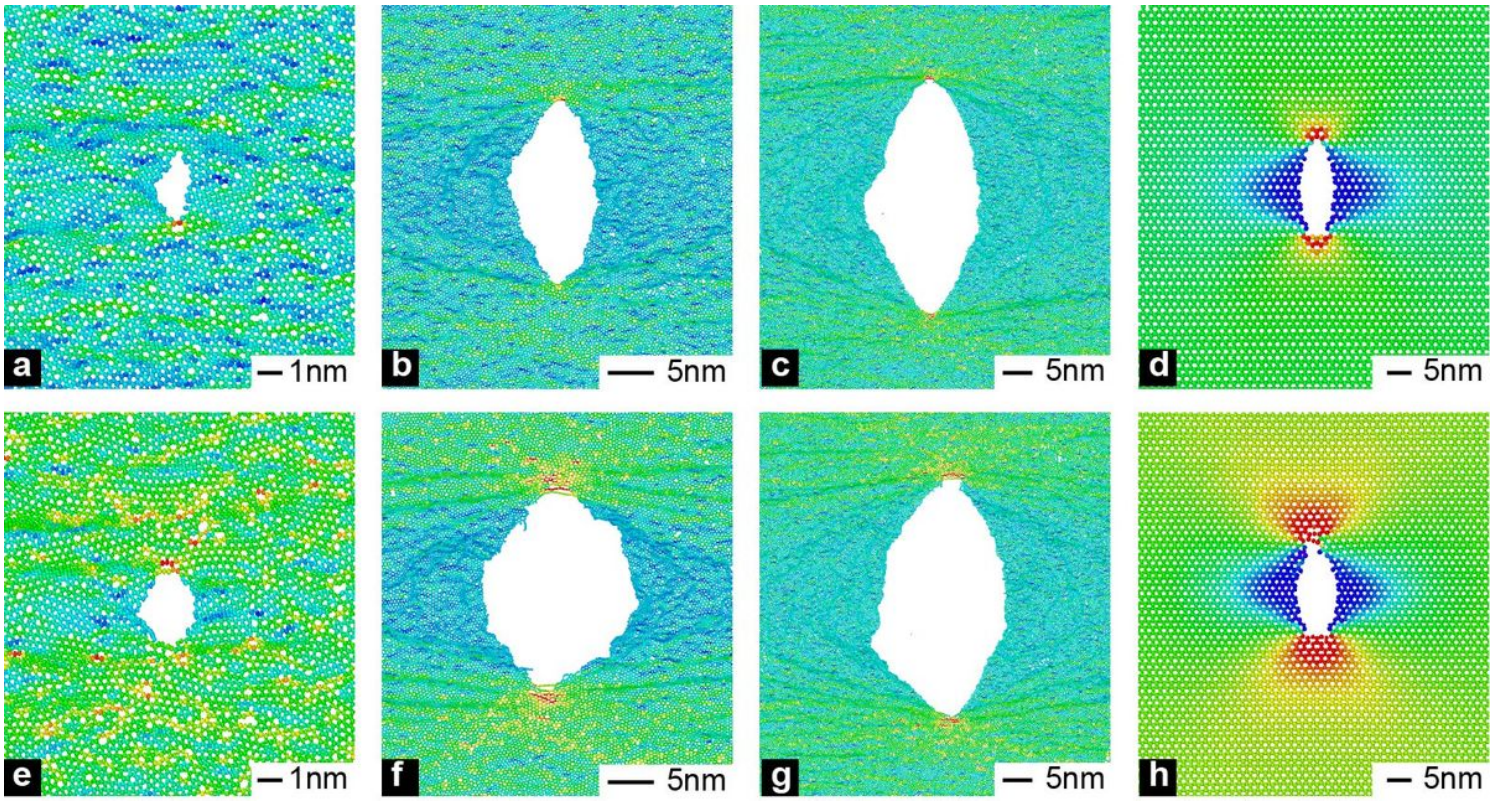

Figure 3

Flaw-tolerance of pre-cracked MAC. (a) to (c) Stress contours at halfway of critical strain for the onset of crack propagation in the pre-cracked MAC, with initial crack length of $2a_0$ = 3 nm, 20 nm, and 40 nm, respectively. (d) Selected reference case of a pre-cracked graphene (initial crack length $2a_0$ = 20 nm). (e) to (h) Stress contours of pre-cracked samples at the onset of crack propagation, corresponding to those of (a) to (d), respectively.

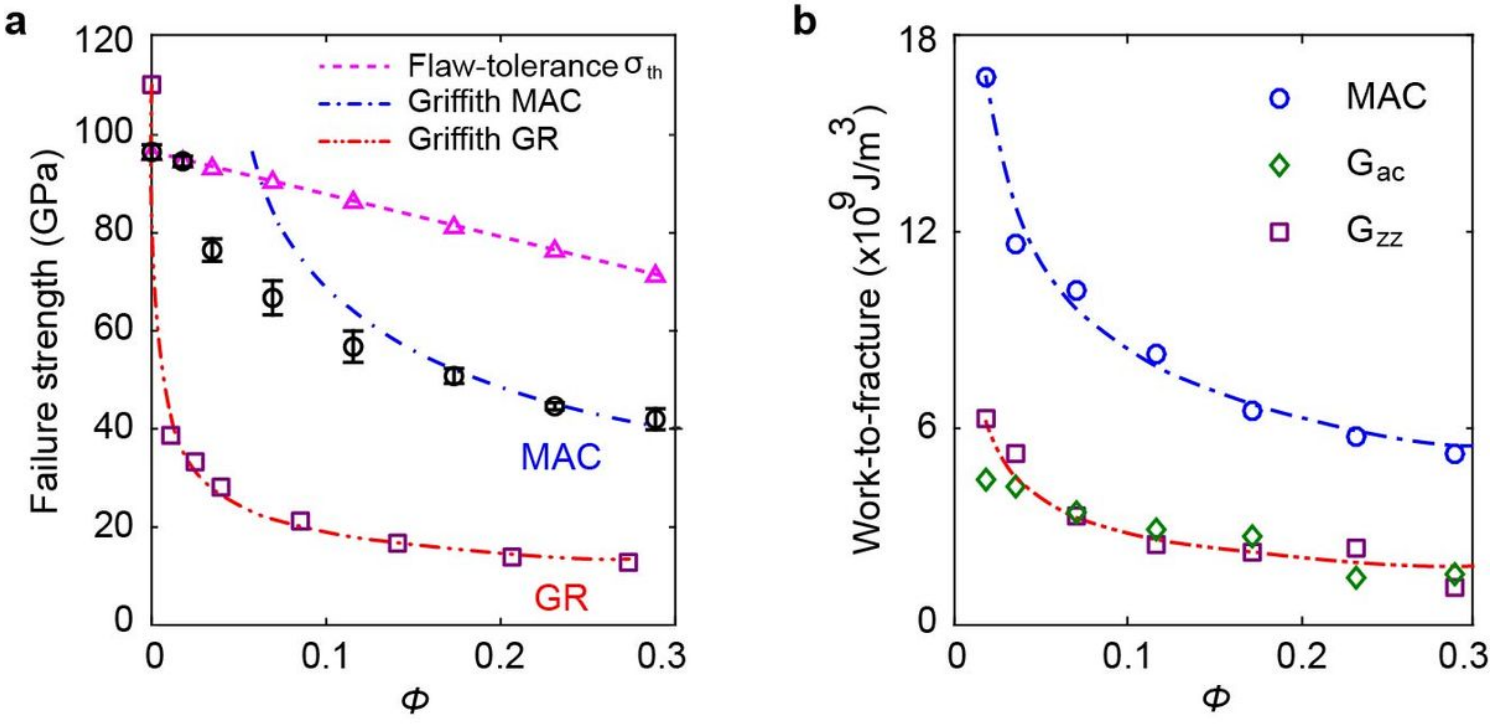

Figure 4

Griffith fracture in MAC and its flaw-tolerance. (a) The failure strength and (b) work-to-fracture as a function of the ratio of crack length to sample width φ. Symbols are data from MD simulations; dash-dotted lines in (a) are Griffith predictions from Eqn. (1), and the dotted line is fitted with $\sigma_{th} = S(1 - \varphi)$. Lines in (b) are fitted for better view. For comparison, the failure strength of pre-cracked graphene from a previous work[30] is also included.

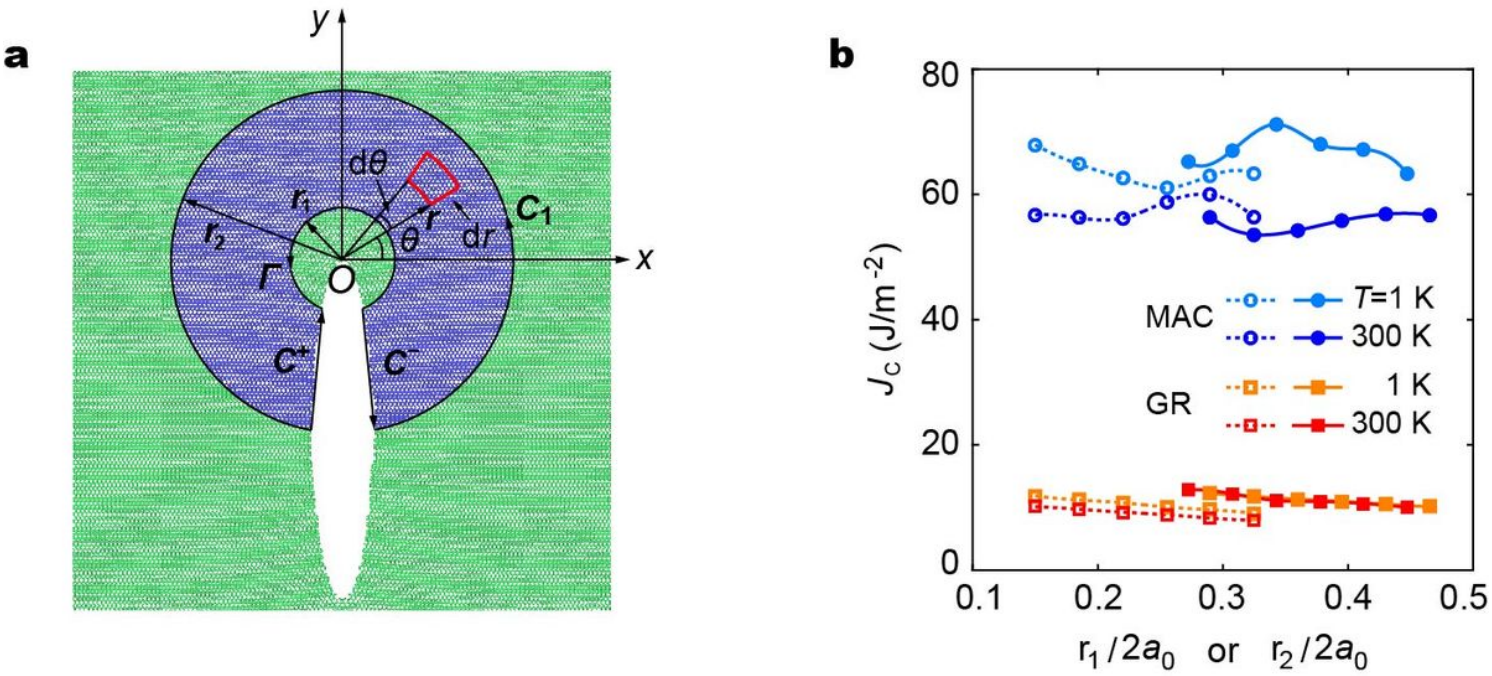

Figure 5

Domain J-integral for pre-cracked MAC. (a) Selected region for domain J-integral and related parameters. (b) The J-integral of pre-cracked MAC (blue lines) and graphene (red lines). To examine the convergence of the domain J-integral, we used a variety of integration domains: by fixing the inner radius $r_1 = 0.3a_0$ while varying r_2 (solid symbols); alternatively, r_1 is allowed to vary while $r_2 = 0.9a_0$ (empty symbols).

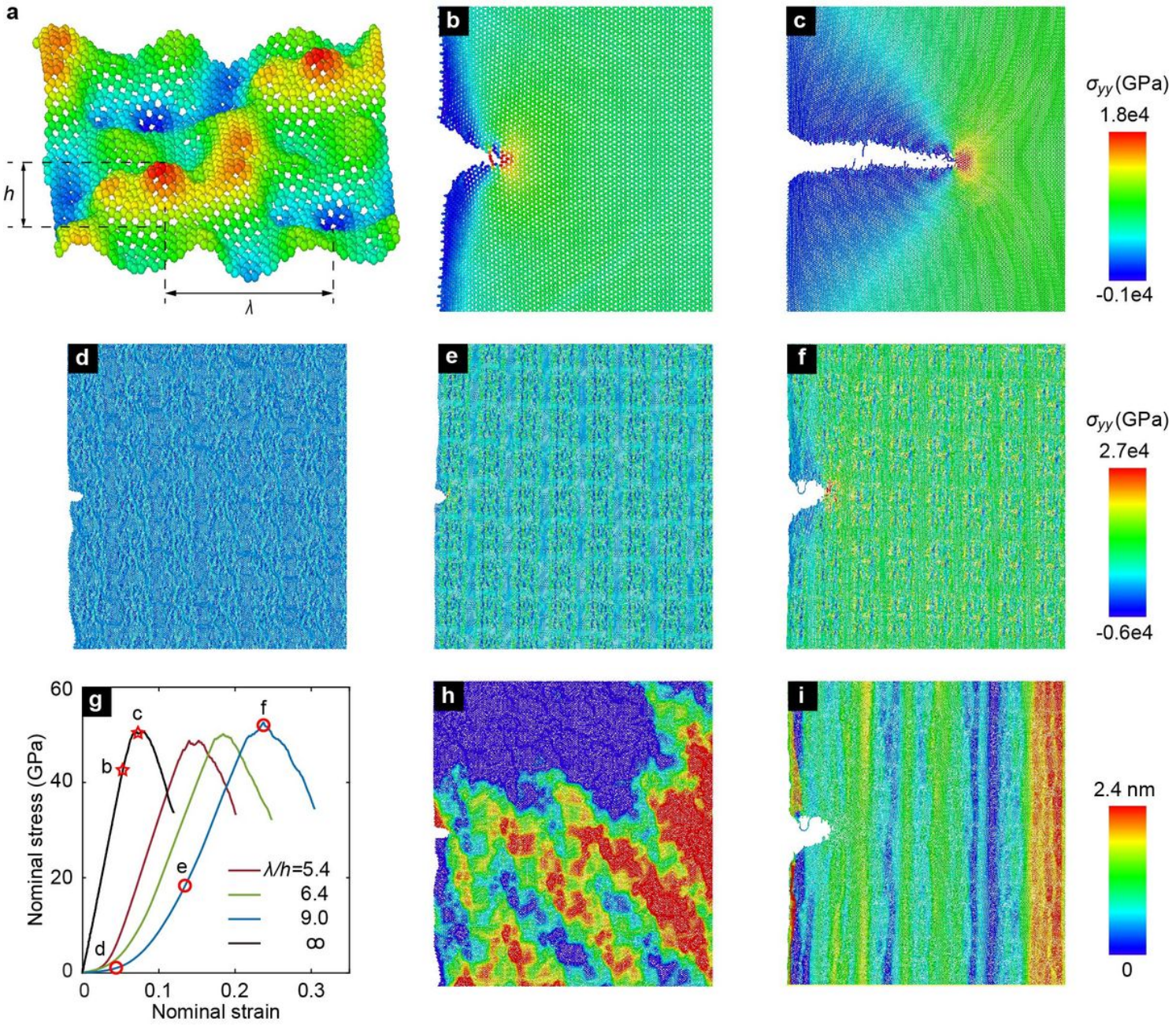

Figure 6

Crack-trapping in domed graphene with an edge-crack . (a) Schematic of a repeating unit of domed structures. (b) to (c) Stress contours of flat graphene at different strains keyed in (g): (b) ε=0.05 and (c) ε=0.07. (d) to (f) Stress contours of sinusoidally domed graphene at different strains keyed in (g): (d) ε=0.05, (e) ε=0.14, and (f) ε=0.23. (h) and (i) Corresponding surface morphologies of (d) and (f), respectively.

Supplementary Files

This is a list of supplementary files associated with this preprint. Click to download.

- SupplementaryInformation.docx
- SupplementaryMovie1.mp4
- SupplementaryMovie2.mp4

- SupplementaryMovie3.mp4
- SupplementaryMovie4.mp4
- SupplementaryMovie5.mp4
- SupplementaryMovie6.mp4